Journal of Applied Electrochemistry **34**: 1085–1091, 2004.

Characterisation of electrodeposited nanocrystalline Ni–Mo alloys

ELISABETH CHASSAING*, NICOLAS PORTAIL, ANNE-FRANCE LEVY and GUILLAUME WANG
*Centre d' Etudes de Chimie Métallurgique-CNRS, 15 rue Georges Urbain, 94407 Vitry-sur-Seine Cedex, France (*author for correspondence, e-mail: elisabeth.chassaing@cecm.cnrs.fr)*

Received 30 January 2004; accepted in revised form 2 June 2004

Key words: electrodeposition, EQCM, Ni–Mo nanocrystalline alloys

Abstract

Ni–Mo nanocrystalline layers were electrodeposited using direct current from citrate–ammonia solutions. The quartz crystal microbalance investigation confirms that the discharge process starts with hydrogen evolution before the onset of the alloy deposition. The grain size was estimated from X-ray line broadening. It decreases when the molybdenum content is increased. It is smaller for layers deposited at pH 9.5 than 8.5. The microhardness exhibits a maximum close to 800 Vickers for τ_{Mo} around 17 wt%. For higher τ_{Mo} a softening is observed showing a deviation from Hall-Petch behaviour due to small grain size. In deaerated hydrochloric solutions, the layers show a large passivation domain without any pitting. The corrosion currents as well as the passivation currents, higher than for the bulk Hastelloy B alloy, decrease when τ_{Mo} is increased.

1. Introduction

In the last decade, nanocrystalline materials have been developed, due to their exceptional mechanical, magnetic, *etc*. properties [1]. Several methods have been proposed for their preparation such as melt spinning, ball milling and gas condensation [1]. Since the pioneering work by Erb et al. [2], investigations on nanocrystalline materials produced by electrodeposition methods have considerably increased. Electrodeposition is a relatively easy and cheap method, in which the initial size of the nuclei can be controlled through the applied overpotential, and leads to dense, non-porous materials, avoiding further compaction.

The electrodeposition of Ni–Mo alloys has been extensively investigated [3–7]. These alloys, such as the commercial alloy Hastelloy B, exhibit exceptional corrosion resistance in highly corrosive media such as non-aerated concentrated hydrochloric solutions [8]. They are also known as good catalysts for hydrogen evolution [9–11]. Although molybdenum cannot be separately deposited in aqueous solutions, it can be co-discharged with an iron-group metal, in the presence of appropriate complexing agents [12]. The codeposition mechanism is still not clearly understood although several investigations have been carried out [4, 13–16].

The goal of the present work is to determine whether the grain size is controlled mainly by the molybdenum content and/or by the electrodeposition conditions and to examine the effect of the grain size on the properties of the films, especially their corrosion resistance. Very limited fundamental understanding exists concerning the corrosion resistance of nanocrystalline materials and controversial results have been published [17].

To this end we prepared a wide range of Ni–Mo alloys of various compositions and investigated their properties in correlation with their grain sizes.

According to literature and previous investigations, the best complexing agent is sodium citrate together with ammonia [3, 7]. The important plating parameters are the ratio of molybdate/nickel species concentrations, the sodium citrate and ammonia (pH) concentrations and the current density. Best results are obtained for pH values in the range 8–10 [3].

2. Experimental conditions

Solutions were prepared from analytical grade purity chemicals dissolved in high-purity water. They contained 0.2 mol dm^3 nickel sulfate, 0.02–0.03 mol dm^{-3} sodium molybdate, 0.2–0.3 mol dm^{-3} trisodium citrate. The composition of the main baths is given in Table 1. The pH was adjusted by addition of ammonia. The bath temperature was maintained at 30 °C. The counter-electrode was a nickel sheet of commercial purity. A saturated calomel reference electrode was used.

Ni–Mo alloys were deposited under galvanostatic conditions on copper foils or on Armco iron plates previously polished and degreased. A quantity of electricity between 200 and 300 C cm^{-2} was applied to obtain a film thickness close to 30 μm. An investigation with an electrochemical quartz crystal microbalance (Maxtek PM 740) was also carried out to obtain more

Table 1. Composition of the main plating solutions (mol dm^{-3})

Electrolyte	$NiSO_4 \cdot 6H_2O$	$Na_2MoO_4 \cdot 2H_2O$	$Na_3C_6H_5O \cdot 2H_2O$	pH
1a	0.2	0.02	0.3	8.5
1b	0.2	0.02	0.3	9.5
2a	0.2	0.03	0.3	8.5
2b	0.2	0.03	0.3	9.5
3a	0.2	0.03	0.2	8.5
3b	0.2	0.03	0.2	9.5

information on the deposition and dissolution characteristics.

The alloy composition was determined either by EDX or ICP analysis. The morphology was observed by SEM. The structure was examined by X-ray diffraction with a cobalt anode ($K_{\alpha 1} = 0.17889$ nm). The size of the coherent domains was estimated from the integral breadth of the diffraction lines using the Scherrer formula. Some TEM observations were also carried out (Akashi EM002B, 200 kV); the samples were first separated from their substrates by peeling or by dissolving the copper foils in chromic acid solutions; the films were further thinned by ion milling. The Vickers microhardness of the deposits was measured with 50–200 g load. The corrosion resistance of the films was determined from the polarisation curves and from impedance measurements in de-aerated 1 N HCl solutions and compared to the behaviour of Hastelloy B.

3. Results

3.1. *Electrodeposition conditions: Composition, current efficiency*

The electrocrystallisation behaviour was investigated by cyclic voltammetry, using an electrochemical quartz crystal microbalance (EQCM). Figure 1 shows the current density response (curves 1) and the mass changes (curves 2) for electrolytes 1a and 1b. With increasing pH, the cathodic polarisation curve is shifted towards more negative potentials (curve 1b compared to curve 1a). This feature is mainly due to the hydrogen evolution reaction, which is much smaller at pH 9.5. In both cases the alloy deposition starts at potentials inferior to -1200 mV SCE^{-1} i.e. about 200 mV smaller than the potential for which the cathodic current starts to increase (curves 2a and b). This behaviour confirms that the cathodic process starts with hydrogen evolution before the onset of metal deposition [7, 13]. We previously showed, through steady-state and impedance investigation, that the deposition of Ni–Mo alloys starts with hydrogen evolution resulting from citrate reduction of the alcohol function, through a mixed oxide layer. When the polarisation is increased, the presence of the Ni^{2+} species enables the reduction of the oxide into the Ni–Mo alloy [13]. It has already been observed for other Co–Mo alloys, that the alloy deposition does not start beyond a certain potential threshold [16].

The partial polarisation curves can be calculated from Figure 1 using Faraday's law and chemical analysis of the alloys (Figure 2). The partial current for molybdenum discharge is increased at pH 9.5 compared to pH 8.5, whereas a marked opposite trend is observed for the nickel discharge.

During the anodic scan, one or two broad peaks are observed. The peak current is the more intense the more cathodic the inversion potential. The peaks are also much more pronounced at pH 8.5 than 9.5 (Figure 1, curve la compared to 1b). Indeed at pH 9.5, the dissolution of the deposited layer is quite low, whereas at pH 8.5 the dissolution of the alloy layer is more intense (curve 2b compared to 2a). In this pH range the alloys never totally dissolve [8].

As is well known in these electrolytes, the molybdenum content, τ_{Mo}, decreases when the current density or the pH is increased (Figure 3, curves 1 and 2). The effect is more pronounced at pH 9.5 than at 8.5. The

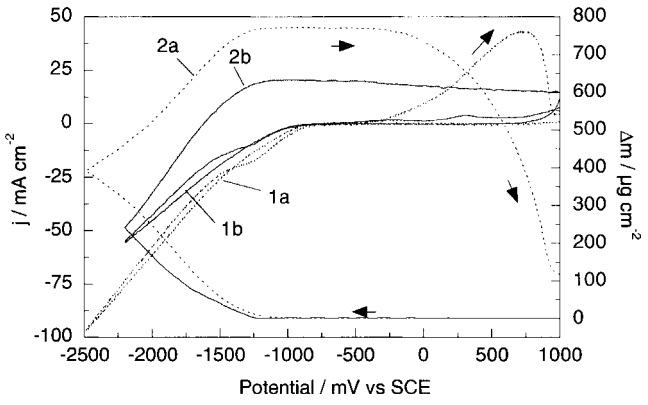

Fig. 1. Cyclic voltammetry curves recorded in the plating solutions using the EQCM (scan rate: 10 m V s^{-1}). Index a (dotted lines): 0.02 M Na_2MoO_4, pH 8.5 (electrolyte 1a); Index b (solid lines): 0.02 M Na_2MoO_4, pH 9.5 (electrolyte 1b). Curve 1: current density responses (mA cm^{-2}); Curve 2: mass changes (μg cm^{-2}).

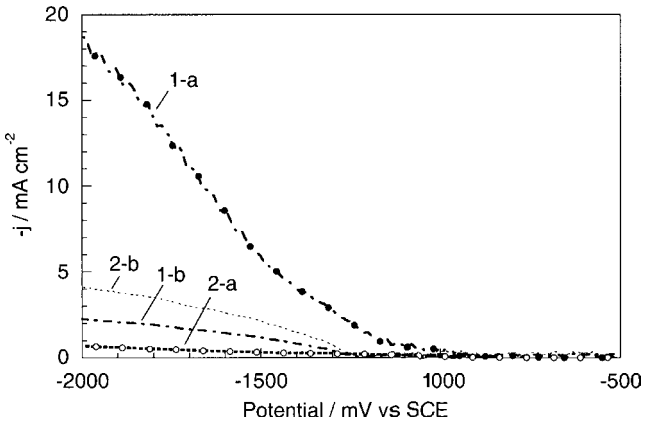

Fig. 2. Partial current densities for nickel and molybdenum discharges (mA cm^{-2}). Curve 1a (electrolyte 1a): Ni partial current density; Curve 2a (electrolyte 1a): Mo partial current density; Curve 1b (electrolyte 1b): Ni partial current density; Curve 2b (electrolyte 1b): Mo partial current density.

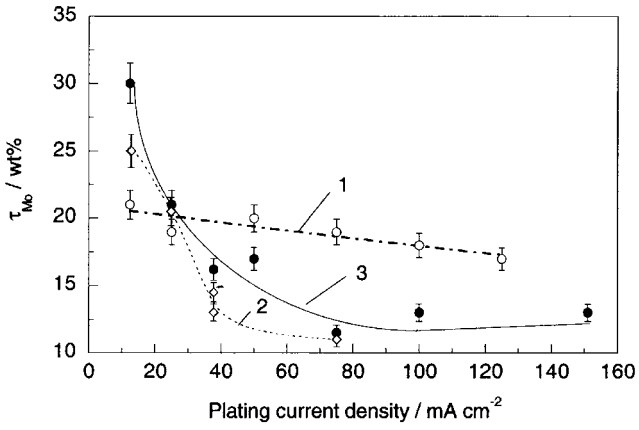

Fig. 3. Molybdenum content as a function of the applied current density. Curve 1: 0.02 M Na_2MoO_4, pH 8.5 (electrolyte 1a); Curve 2: 0.02 M Na_2MoO_4, pH 9.5 (electrolyte 1b); Curve 3: 0.03 M Na_2MoO_4, pH 9.5 (electrolyte 2b).

molybdenum content increases slightly with the molybdate concentration in the solution (curves 2 and 3). The current efficiency ranges from 70 to 30%, it decreases for current densities higher than 20 mA cm^{-2}, or when the pH is reduced or when the molybdate or the citrate concentration is increased.

For this investigation, several Ni–Mo films have been prepared in a wide range of compositions from 5 to 40 wt % Mo, by varying the deposition conditions. Alloys with high molybdenum contents have been deposited under forced hydrodynamic conditions.

3.2. *Surface morphology*

Films deposited at low current densities are bright and show a light grey colour. As examined by SEM, they exhibit a more or less nodular morphology. The size of the nodules depends on the deposition conditions; it is smaller at pH 9.5 (Figure 4a) than at pH 8.5 (Figure 4b). The alloys with a molybdenum content higher than 30 wt % often exhibit cracks due to high tensile stress levels [3] (Figure 4c).

3.3. *Crystalline structure*

The layers exhibit the face-centred-cubic structure of the Ni–Mo solid solution, supersaturated for films with molybdenum content higher than about 20 wt % [18]. At low molybdenum content, the XRD patterns show all the characteristic diffraction peaks (Figure 5). With increasing molybdenum content, τ_{Mo}, the lines are increasingly broadened and their intensities decrease; the (1 1 1) preferred orientation becomes more pronounced. For large molybdenum content, quasi-amorphous alloys are obtained and only the (1 1 1) halo is observed.

The grain size, or more precisely the size of the coherent domains, was calculated from the line broadening, corrected for device broadening, using Scherrer's formula. Due to the marked preferred orientation, only the (1 1 1) line was used and hence Williamson and Hall or Halder Wagner analysis was not possible. As a result, the grain size may be underestimated since microstresses,

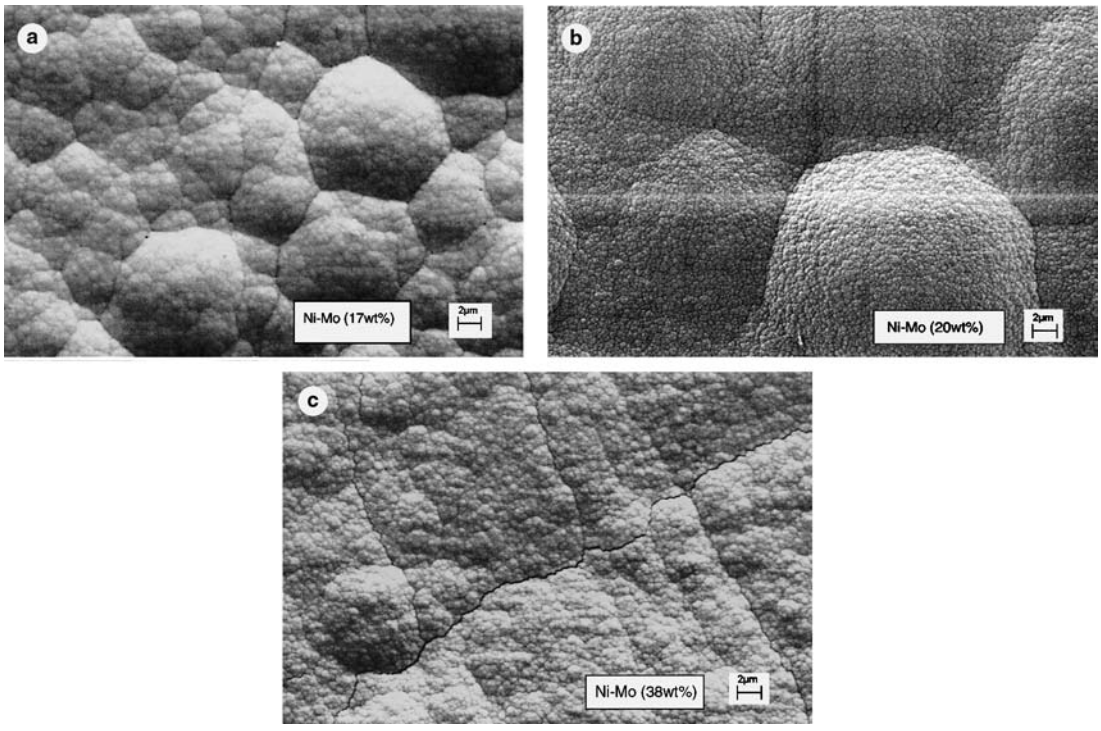

Fig. 4. SEM micrographs (secondary electron images). (a) Ni–Mo (17 wt %) (electrolyte 3b, 150 mA cm^{-2}, thickness 22 μm); (b) Ni–Mo (20 wt %) (electrolyte 1a, 60 mA cm^{-2}, thickness 35 μm); (c) Ni–Mo (38 wt %) (electrolyte 1b, 150 mA cm^{-2}, thickness 28 μm).

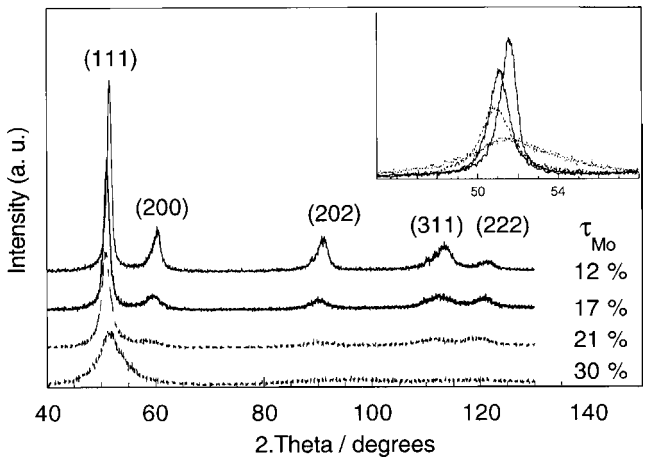

Fig. 5. XRD patterns for Ni–Mo layers deposited from solution containing 0.03 M Na_2MoO_4 at pH 9.5 (electrolyte 2b).

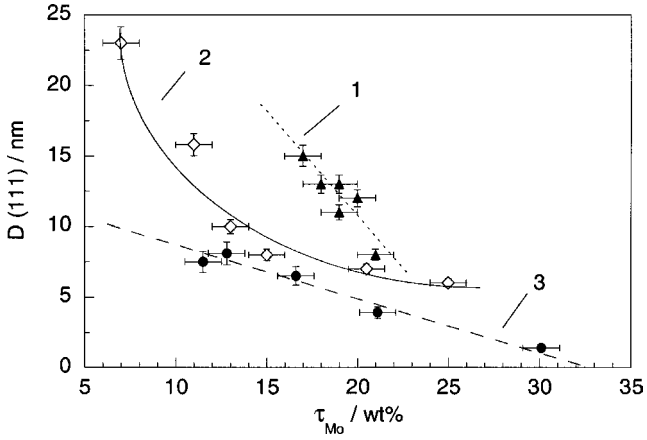

Fig. 6. Grain size (coherency length along, ⟨1 1 1⟩ direction) of Ni–Mo layers as a function of molybdenum content. Curve 1: 0.02 M Na_2MoO_4, pH 8.5 (electrolyte 1a); Curve 2: 0.02 M Na_2MoO_4, pH 9.5 (electrolyte 1b); Curve 3: 0.03 M Na_2MoO_4, pH 9.5 (electrolyte 2b).

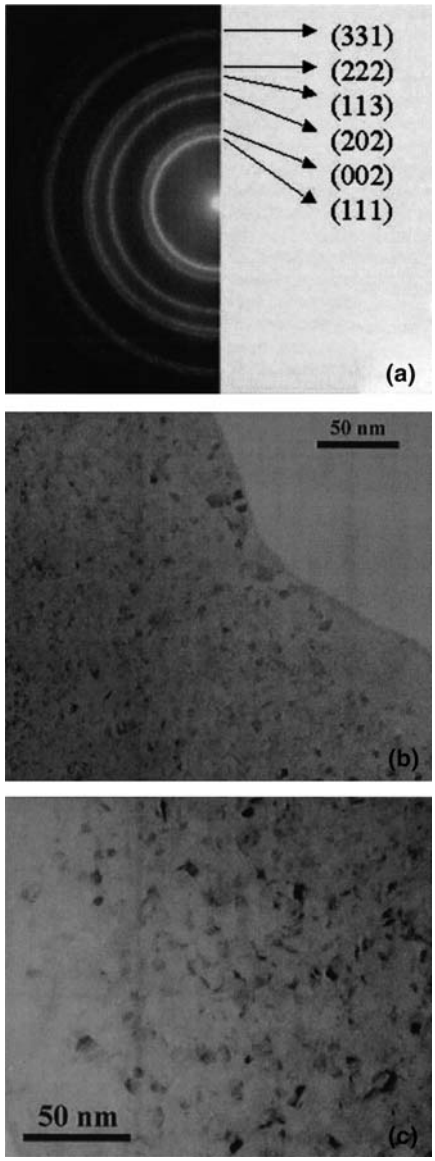

Fig. 7. TEM images Ni–Mo alloys deposited from electrolyte 2b. (a) electron diffraction of Ni–Mo 30 wt %; (b) bright field images of Ni–Mo 30 wt%; (c) bright field images of Ni–Mo 21 wt %.

which also contribute to the line broadening are probably important. As shown in Figure 6, the grain size decreases markedly from 25 nm to a few nm when the molybdenum content increases from 10 to 35 wt %. Quasi-amorphous alloys are obtained for τ_{Mo} greater than 30 wt %. However, the grain size is larger for alloys deposited at pH 8.5 than at pH 9.5 (curves 1, 2 and 3). It may be noted that the grain sizes are much smaller than those obtained for pure nickel layers, pulse-plated in the absence of additives, which were around 30 nm [2].

3.4. *TEM investigation*

Figure 7(a) shows an electron diffraction diagram of Ni–Mo alloy thin film with 30 wt % Mo. The diffraction rings are characteristic of the polycrystalline fee structure of this alloy. Figure 7(b) and (c) shows bright field images of Ni–Mo alloys with 30 and 21 wt % Mo. In this case, the electron diffraction by crystallites is responsible for image contrast: the dark particles represent crystallites in diffraction position, the bright areas correspond to crystallites out of diffraction condition. These images exhibit grain sizes ranging between 4 and 17 nm with certain dispersion (average 5 nm). This grain size is slightly greater than the coherency length measured by X-ray diffraction as explained above.

3.5. *Microhardness*

The microhardness of the electrodeposited alloys is in the range 500–800 HV. As often observed for electrodeposited films, this value is much higher than for the bulk alloy Hastelloy B (290 ± 10 HV). No monotonic dependency, neither with the molybdenum content, nor with the grain size is observed (Figure 8). For grain sizes in the range 10–15 nm, the microhardness increases with

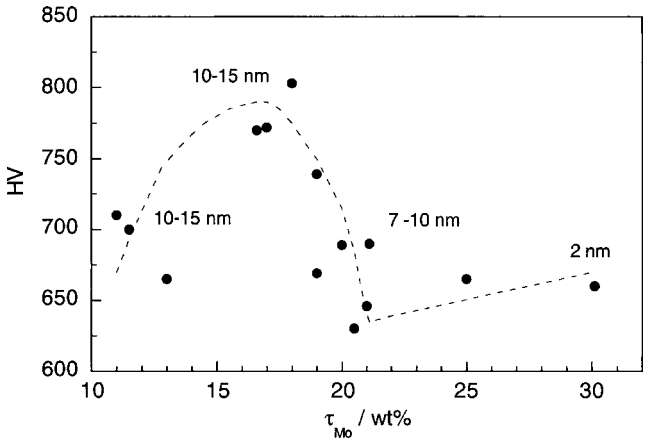

Fig. 8. Microhardness of various Ni–Mo deposits as a function of molybdenum content, τ_{Mo}. Indices indicate the corresponding grain sizes (the dashed line is only a guide for the eyes).

molybdenum content. A maximum is obtained for 16 ± 1 wt % Mo. For higher τ_{Mo}, HV decreases with increasing τ_{Mo} and decreasing grain size.

According to the Hall-Petch relationship, the hardness should increase when the grain size, D, decreases as a function of D^n, with n close to -0.5 [1]. In the case of Ni–Mo alloys, hardness is also expected to increase when the Mo content is increased. Figure 9 shows the microhardness plotted as a function of $D^{-0.5}$. For grain size greater than 10 nm, the microhardness follows a Hall-Petch behaviour (solid line). For smaller grain size, deviation is observed, as already shown for Ni or Ni–W electrodeposited nanocrystalline materials [2, 19, 20].

We applied a model proposed by Palumbo et al. [21] to evaluate the grain size dependence of volume fractions associated with grain boundaries and triple junctions, which considers the grain shape as regular 14 sided tetrakaidecahedron. The total intercrystalline fraction (V_{ic}) would be given by $V_{ic} = 1 - [(D - \Delta)/D]^3$ and the volume fraction of the grain boundary fraction (V_{gb}) is: $V_{gb} = [3\Delta(D - \Delta)]^2/D^3$, where D is the mean grain size and Δ, the grain boundary thickness (1–2 nm for nanocrystalline deposits [19]). The volume fraction associated with the triple junction would then be equal to the difference $V_{tj} = V_{ic} - V_{gb}$. For example, for a grain size of 15 nm, intercrystalline regions occupy about 19% of the surface area, if we assume a grain boundary thickness of 1 nm ($V_{ic} = 35\%$ for $\Delta = 2$ nm). The onset of decreasing hardness would occur when the intercrystalline regions, especially the triple lines, occupy an significant fraction of the material [2].

We made a rough estimate of the hardness grain size dependency as developed by Yamasaki et al. for Ni–W nanocrystalline deposits [19]. For mean grain size, D, greater than 10 nm, the hardness follows Hall-Petch behaviour (Figure 9, solid line). For smaller grain sizes, deviation occurs. The hardness, H_{cal}, would vary as a function of the total intercrystalline fraction (V_{ic}), rather than the triple junction fraction according to: $H_{cal} = V_{ic} H_{ic} + (1 - V_{ic}) H_{HP}$, where H_{HP} is the Hall-Petch hardness (slope 0.6 MPa $m^{-0.5}$, i.e. lower than for Ni–W alloys [19]) and H_{ic} is the hardness of amorphous materials (estimated as 770 HV). Figure 9 (dashed line) shows that the experimental data qualitatively agree with this fit.

3.6. *Corrosion resistance*

The corrosion resistance of the electrodeposited alloys was measured in deaerated 1 M HCl solutions, in which Ni–Mo alloys are known to exhibit excellent corrosion resistance [8]. Their behaviour is compared to that of Hastelloy B. The results are summarised in Table 2. We first investigated the corrosion resistance of these alloys using the quartz crystal microbalance. Ni–Mo films (20 wt % Mo) were electrodeposited on the EQCM from electrolyte 1a. Figure 10 shows the current density (curve 1) and the mass responses (curve 2). Tafel extrapolation

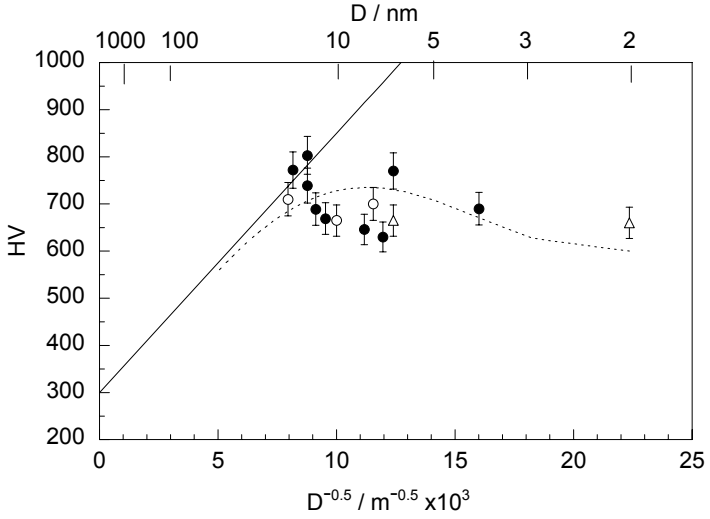

Fig. 9. Microhardness of various Ni–Mo deposits as a function of D^{-05}, (D mean grain size) (solid line: Hall-Petch relationship, dashed line: H_{cal}). (○) τ_{Mo} = 11–13 wt % Mo; (●) τ_{Mo} = 16–20 wt % Mo; (△) τ_{Mo} = 25–30 wt % Mo.

Table 2. Molybdenum content, τ_{Mo}, grain size, D, corrosion current density, J_{corr}, corrosion potential, E_{corr}, passive current density, J_p and breakdown potential, $E_{breakdown}$

Experimental conditions	τ_{Mo}/wt%	D/nm	$J_{corr}/\mu A\ cm^{-2}$	E_{corr} vs SCE/mV	$J_p/\mu A\ cm^{-2}$	$E_{breakdown}$ vs SCE/mV
HastB	28		30	−270	15	−30
Ni–Mo/EQCM	20		85	−220	90	−50
Ni–Mo/EQCM	20		90	−230	60	−10
Electrolyte 2b	11.5	7.5	420	−300	200	−40
	13	8	250	−295	130	−40
	17	6.5	150	−300	120	−40
	21	4	60	−295	100	−50
	30	1.5	55	−300	100	−50
Electrolyte 1a	21	8	160	−280	90	−20
	19	11	120	−275	65	−10
	20	12	140	−260	90	−20
	19	13	175	−275	100	−10
	18	13	400	−290	190	−10
	17	15	1000	−300	300	−10
Electrolyte 1b	15	8	35	−325	65	−20
	7	23	3500	−325	620	−60
Electrolyte 3b	7	12	2800	−310	500	−100
	38[a]	2	2000	−330	450	−60

[a] This layer showed several cracks

of the cathodic polarisation curve leads to a corrosion current density close to 85 μA cm^{-2}, i.e. higher than for Hastelloy B (30 μA cm^{-2}). In the anodic range, the deposit shows a large passivation domain. For potentials greater than about −50 mV, transpassive dissolution occurs. No pitting and no hysteresis on the reverse scan are observed (see insert in Figure 10). We calculated $R = \Delta m_{exp} \cdot F/Q$, ratio of the experimental mass decrease times the Faraday's constant divided by the electrical charge. According to Faraday's law, this ratio is the equivalent molar mass of the dissolving material, provided that the faradic efficiency is equal to unity. In the potential range −0.1 to 0 V, this ratio is constant and equal to 26 ± g^{-1} mol^{-1}, which is approximately the equivalent molar mass of a 20 wt % Mo alloy. This confirms that, in this potential range, transpassive dissolution of the alloy occurs. Figure 11 shows examples of polarisation curves for some deposits together with that of Hastelloy B. All the samples exhibit a passivation behaviour with a breakdown potential in the range −50 to −10 mV (Table 2). The corrosion current density and the passive current density are markedly higher than for the bulk alloy, Hastelloy B. Both currents decrease when the molybdenum content increases. However, these currents also depend on the grain size, as shown for the corrosion current in Figure 12.

For nanocrystalline nickel it has been shown that, though the thickness and composition of the passive

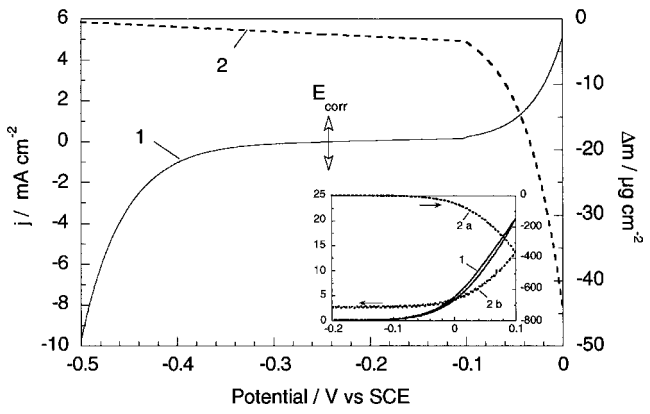

Fig. 10. Voltammetric behaviour in de-aerated 1 N HCl solution of a Ni–Mo layer (20 wt %) deposited from electrolyte 1b on the EQCM (scan rate: 1 mV s^{-1}). Curve 1: current density response; Curve 2: mass change response. Insert: forward and reverse scans in the potential range −0.2, +0.1 V.

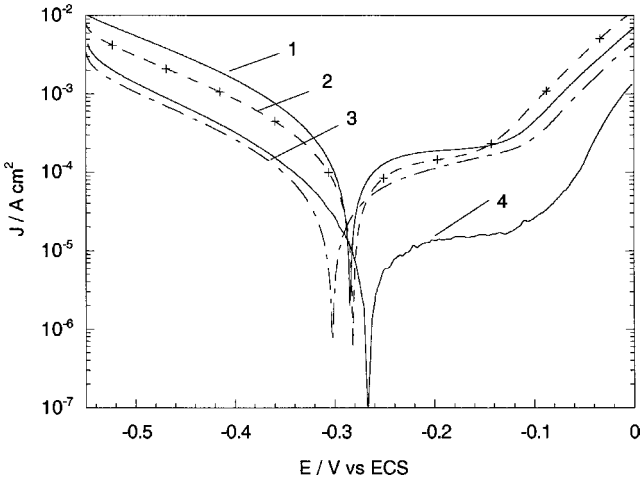

Fig. 11. Polarisation curves of various Ni–Mo deposited from solution 0.03 M Na_2MoO_4, pH 9.5 (electrolyte 2b). Curve 1: τ_{Mo} = 12 wt%; Curve 2: τ_{Mo} = 17 wt%; Curve 3: τ_{Mo} = 30 wt%; Curve 4: Hastelloy B.

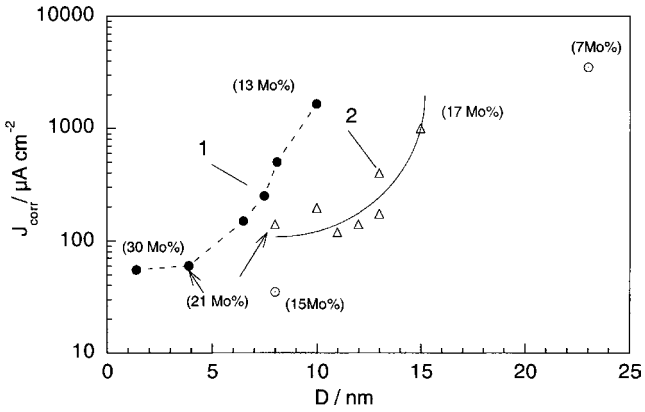

Fig. 12. porrosion current density as a function of grain size. Curve 1: 0.03 M Na_2MoO_4, pH 9.5 (electrolyte 2b); Curve 2: 0.02 M Na_2MoO_4, pH 8.5 (electrolyte 1a); (⊙) 0.02 M Na_2MoO_4, pH 9.5 (electrolyte 1b).

films are nearly identical as for macrocrystalline nickel, the passive current density was higher and increases when the grain size decreases [22–24]. This was attributed to the higher proportion of default sites, i.e. grain boundaries and triple junctions in the nanocrystalline metals. Again we applied Palumbo's model to the passivation behaviour of the Ni–Mo deposits. Taking account of the grain size, we decomposed the passivation currents, J_p, into a partial current associated with the grain boundary, $J_{gb} = J_p * V_{gb}$ and an intrinsic passivation current $J_{intrinsic} = J_p - (J_p * V_{gb})$. Figure 13 shows an example of this qualitative calculation. The intrinsic passivation current, $J_{intrinsic}$, depends on the alloy composition (curve 2) whereas the current density associated with the grain boundaries is nearly constant and close to 50 μA cm^{-2} (curve 3).

4. Conclusion

Ni–Mo alloys have been electrodeposited using direct current. The grain size of the alloys decreases when the molybdenum content is increased. However, it also depends on the deposition conditions; it decreases when the electrolyte pH or the molybdate concentration is increased (Figure 6).

The corrosion behaviour appears to depend on both parameters: molybdenum content and grain size, which controls the grain boundary volume fraction. When the Mo content is increased, the intrinsic corrosion resistance tends to increase, but the grain size is reduced and hence the fraction of intercrystalline regions increases drastically, which has an opposite effect. The best corrosion resistance is obtained for alloys with 15–30 wt % Mo. Larger molybdenum contents induce cracking of the films leading to non-protective coatings. For lower molybdenum content, films with the smaller grain size have the best corrosion resistance.

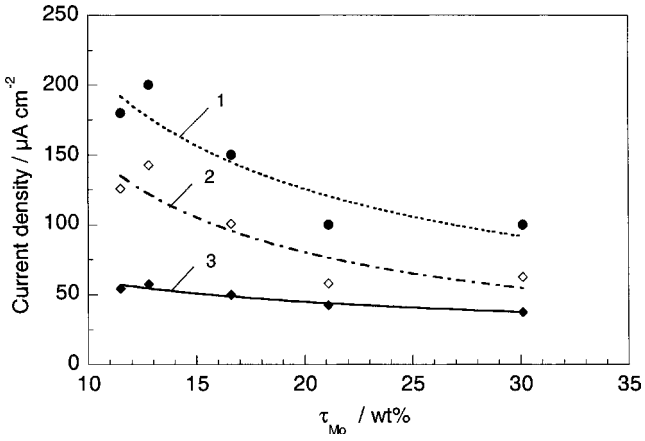

Fig. 13. Passive behaviour as a function of molybdenum content (electrolyte 2b). Curve 1: Passivation current density, J_p; Curve 2: $J_{intrinsic} = J_{gb} - J_p$; Curve 3: J_{gb} calculated according to [21].

References

1. C. Suryanarayana, *Int. Mat. Rev.* **40** (1995) 41 and references therein.
2. U. Erb, A.M. El-Sherik, G. Palumbo and K.T. Aust, *Nanostruct. Mater.* **2** (1993) 383.
3. E. Chassaing, M.P. Roumegas and M.F. Trichet, *J. Appl. Electrochem.* **25** (1995) 667.
4. E.J. Podlaha, M. Matlosz and D. Landolt, *J. Electrochem. Soc.* **140** (1993) L149.
5. S. Rengakuji, Y. Nakamura, N. Sumi, K. Nishibe and T. Komura, *Denki Kagaku* **63** (1995) 400.
6. Y. Zeng, Z. Li, M. Ma, S. Zhou, *Electrochem. Comm.* **2** (2000) 36.
7. L.S. Sanches, S.H. Domingues, A. Carubelli and L.H. Mascaro, *J. Brazilian Chem. Soc.* **14** (2003) 556.
8. W.Z. Friend, in Corrosion of Nickel and Nickel-base Alloys (Wiley-Interscience publication, New York, 1980), p. 248.
9. C.L. Fan, D.L. Piron, A. Sleb and P. Paradis, *J. Electrochem. Soc.* **141** (1994) 382.
10. Y.C. Chang, K.C. Fan and C.I. Lin, *J. Chin. Inst. Chem. Eng.* **33** (2002) 499.
11. T. Sato, H. Takahashi, E. Matsubara and A. Muramatsu, *Mat. Trans.* **43** (2002) 1525.
12. A. Brenner, in Electrodeposition of Alloys, Vol. II Academic Press, 1963, pp. 347–408.
13. E. Chassaing, K. Vu Quang and R. Wiart, *J. Appl. Electrochem.* **19** (1989) 839.
14. S. Rengakuji, Y. Nakamura, K. Nishibe, M. Inoue and T. Komura, *Denki Kagaku* **62** (1994) 602.
15. E.J. Podlaha and D. Landolt, *J. Eectrochem. Soc.* **144** (1997) 1672.
16. E. Gomez, E. Pellicer and E. Valles, *J. Appl. Electrochem.* **33** (2003) 245.
17. C. Suryanarayana and C.C. Koch, *Hyperfine Interact.* **130** (2000) 5.
18. W.B. Pearson, A Handbook of Lattice Spacings and Structures of Metals and Alloys, Vol. 2 (Pergamon Press, 1967).
19. T. Yamasaki, P. Schlossmacher, K. Ehrlich and Y. Ogino, *Nanostruct. Mater.* **10** (1998) 375.
20. T. Yamasaki, R. Tomohira, Y. Ogino, P. Schlossmacher and K. Ehrlich, *Plating Surf. Finish.* **87** (2000) 148.
21. G. Palumbo, S.J. Thorpe and K.T. Aust, *Scri. Met. et Mat.* **24** (1990) 1347.
22. R. Rofagha, R. Langer, A. M. El-Sherik, U. Erb, G. Palumbo and K.T. Aust, *Scri. Met. et Mater.* **25** (1991) 2867.
23. R. Rofagha, U. Erb, D. Ostrander, G. Palumbo and K.T. Aust, *Nanostruct. Mater.* **2** (1993) 1.
24. R. Rofagha, S.J. Splinter, U. Erb and N. S. McIntyre, *Nanostruct. Mater.* **4** (1994) 69.